BIOMIMETICS

Light-stimulated actuators based on nickel hydroxide-oxyhydroxide

K. W. Kwan, S. J. Li, N. Y. Hau, Wen-Di Li, S. P. Feng, Alfonso H. W. Ngan*

Light-induced actuators that are self-contained and compact can be used as artificial muscles for microrobotics because their actuation can be induced wirelessly, which reduces the complexity of the device or system. Here, we report a material system, nickel hydroxide-oxyhydroxide, that could actuate because of a volume change stimulated by illumination of visible light of low intensities. The actuating material here exhibited a turbostratic crystal structure capable of intercalating water, and we show that the intercalated water can be rapidly and reversibly desorbed into the environment under visible light of low intensities, resulting in fast actuation driven wirelessly by light. By electroplating the actuating material on passive substrates, we have fabricated film actuators capable of undergoing reversible bending and curling with an intrinsic actuating stress of 5 to 65 megapascals at response rates in the order of tens to hundreds of degrees per second depending on the light intensity, which are comparable to mammalian skeletal muscles. By intentionally electroplating the nickel hydroxide-oxyhydroxide on selected areas of the substrate, a hinged actuator that can lift objects ~100 times the weight of the actuating material is achieved. Other demonstrations show the potential uses in robotic devices, including sunlight-induced actuation, a biomimicked "sensitive plant" with rapid leaf movement, and a light-powered walking bot.

INTRODUCTION

Actuating materials operating as artificial muscles in robotic applications that can rival skeletal muscles in mammals are being intensively sought (*1*, *2*). Such materials should be able to actuate intrinsically under certain stimuli in a self-contained way, without the need of mechanical components such as gears, pulleys, or belts. Many material systems are capable of producing actuation when driven by electricity, but then, electrical wiring and additional components, such as electrolyte and electrodes, are required (*3*–*11*), which would limit their applications.

Therefore, materials capable of producing actuation when stimulated by light are of great interest because they can offer tremendous potential in applications as wireless actuators (*12*, *13*) for microrobots (*14*, *15*). A few materials have been found to have light-triggered actuation properties, but most of these are powered by ultraviolet (UV) (*16*–*23*) or near-infrared (NIR) light (*24*–*27*). Other light-sensitive materials have very slow actuation responses that may take tens of seconds to fully actuate (*28*–*30*), or they require very high light intensities (*31*) yet produce rather low actuating stress (*32*). In this article, we report a very substantial light-stimulated actuation effect of the nickel hydroxide-oxyhydroxide [$Ni(OH)_2$-NiOOH] material system that operates under visible (Vis) light of low intensities.

The $Ni(OH)_2$-NiOOH redox couple was previously exploited for use in rechargeable battery electrodes (*33*) and was recently studied for an electrochemical actuation effect upon electric potential charging through an alkaline electrolyte (*34*). $Ni(OH)_2$-NiOOH is also known to be water-swelling, although it appears to be dry, because it can retain water molecules between the crystal planes in a turbostratic structure (*35*), in which the planes along the *c* axis are tilted and rotated because of the intercalation of water molecules, as shown in Fig. 1A (*36*). Here, we show that $Ni(OH)_2$-NiOOH can produce remarkable actuation due to removal of the intercalated water molecules by light illumination alone, without the need of any electrical contact or electrochemical cell setup. We have fabricated skin-effect actuators comprising an active $Ni(OH)_2$-NiOOH layer supported by a passive substrate, and these can actuate quickly at 30°/s by visible (Vis) light of a low intensity of 5 mW/cm^2. At higher intensities of 10 to 100 mW/cm^2, the $Ni(OH)_2$-NiOOH could respond at a rate of 60°/s to 400°/s and produce an actuating stress of 30 to 65 MPa that is comparable to mammalian skeletal muscles (*1*), thus allowing it to lift an object ~100 times heavier than its own weight.

Department of Mechanical Engineering, the University of Hong Kong, Hong Kong.
*Corresponding author. Email: hwngan@hku.hk

RESULTS

Materials characterization

The $Ni(OH)_2$-NiOOH film actuators, composed of layers of nickel (Ni), gold (Au), and $Ni(OH)_2$-NiOOH, were fabricated by three-step electroplating (fig. S1A). The actuators were adhered at one end to a copper (Cu) tape for actuation tests (Fig. 1B). Their sizes were about 18 mm by 4 mm, and the thicknesses of the $Ni(OH)_2$-NiOOH layers and substrates were measured by a profilometer to be 1.0 ± 0.2 and 1.3 ± 0.2 μm, respectively. Without any treatment, the as-plated $Ni(OH)_2$-NiOOH was in an oxidized state. To also study the reduced state of the material, we reduced a batch of the plated actuators in 1 M sodium hydroxide (NaOH) at −0.4V, which turned the color of the $Ni(OH)_2$-NiOOH from gray to golden. By plating at selected areas (fig. S1B) and patterned plating (fig. S1C), we fabricated actuators with actuating hinges and biomimicking configurations.

Cyclic voltammetry (CV) performed on a typical fabricated actuator under 1 M NaOH (fig. S2) shows the characteristic oxidation and reduction peaks of the $Ni(OH)_2 \leftrightarrow$NiOOH couple (*37*). As the electric potential approached the values corresponding to the oxidation and reduction peaks in the CV, electrochemical actuation due to the redox reaction occurred as reported earlier (*34*). Such electrochemical actuation behavior of an actuator with the $Ni(OH)_2$-NiOOH facing right is demonstrated in fig. S3 and movie S1. It can be seen that, as the potential was scanned from 0 to 0.6 V, the actuator bent and curled in the direction that corresponded to the contraction of the $Ni(OH)_2$-NiOOH layer, which is hereafter defined as the "forward" direction. On the other hand, when the potential was reduced from 0.6 to 0 V, the actuator returned to the original position by bending and curling in a "backward" direction corresponding to the expansion of the $Ni(OH)_2$-NiOOH active layer.

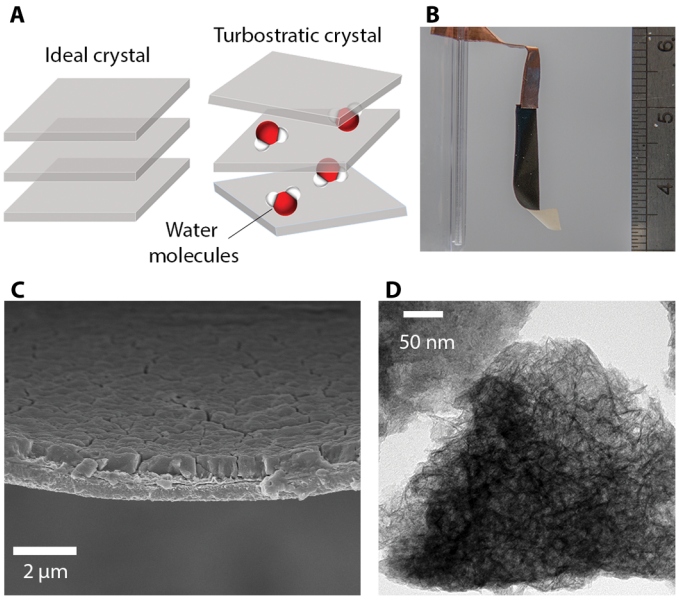

Fig. 1. Characteristics of the $Ni(OH)_2$-NiOOH actuator. (**A**) Schematic diagram of the $Ni(OH)_2$-NiOOH turbostratic crystal structure in which water molecules intercalated between the crystal planes. (**B**) Photo of the actuator and (**C**) its cross section in SEM exhibiting a layered structure. (**D**) TEM image of $Ni(OH)_2$-NiOOH showing a crumpled microstructure.

Scanning electron microscopy (SEM) shows that the $Ni(OH)_2$-NiOOH layer resided on a substrate comprising a thin layer of Au (Fig. 1C) on top of a Ni layer. A top-view SEM image of the $Ni(OH)_2$-NiOOH and the underlying Au layer is shown in fig. S4. The surface of the $Ni(OH)_2$-NiOOH was rough, and the deposited Au appeared as a closed packing of nanoflakes. The overall elemental composition of the cross section was measured by energy-dispersive x-ray spectroscopy (EDS) to be 13% O, 69% Ni, 15% Au, and 3% Co, and the EDS map of the cross-section of an actuator in fig. S5 indicates a distinctive oxygen-rich layer on top of an Au and a Ni layer. These results show that the substrate was made of Ni and Au of about 1 μm and 100 nm, respectively, and that the oxygen-rich layer on top was $Ni(OH)_2$-NiOOH, as confirmed by other characterization techniques detailed below.

Transmission electron microscopy (TEM) shows that the microstructure was crumpled (Fig. 1D), which is characteristic of the turbostratic structure of $Ni(OH)_2$-NiOOH (*36*). The turbostratic structure is further confirmed by selected area electron diffraction (SAED) in fig. S6, which shows dispersed rings for both the oxidized and reduced states (*36*). The diffraction rings of the SAED give interplanar spacings of 2.4 and 1.4 Å for an oxidized sample and 2.6 and 1.6 Å for a reduced one. The former roughly match the (002) and (110) planes of β-NiOOH or (102) and (110) of γ-NiOOH, and the latter match the (100) and (110) of β-$Ni(OH)_2$ or (110) and (301) of α-$Ni(OH)_2$ (*38*, *39*).

Glazing-incidence x-ray diffraction (GIXRD) spectra of the oxidized and reduced sample shown in fig. S7 also confirmed the turbostratic structure of the material, because the resultant peaks are broad and asymmetric (*40*). The 2θ values for the peaks of the oxidized sample are 37° and 66°, which correspond to the interplanar spacings of 2.4 and 1.4 Å, and those for the reduced sample are 34° and 61°, corresponding to 2.6 and 1.5 Å, which match well with the measurement from SAED. All these confirm that the electroplated material was turbostratic $Ni(OH)_2$-NiOOH. The spectra remained unchanged when the samples were illuminated by Vis light at 10 mW/cm^2 during the GIXRD measurements, showing that the light did not induce any redox reaction.

Light-induced actuation mechanism

When illuminated by light, the presented actuators exhibited a significant actuation behavior not reported before. Figure 2A shows the actuation response under UV, Vis, and NIR light illumination performed in an experimental setup shown in fig. S8. Vis light was able to curl the actuator significantly, whereas UV and NIR light triggered milder actuation. The response of the light-induced actuation was instantaneous, and the actuator started to recover once the light was turned off (movie S2). The observation that the actuator responded best to Vis light agrees well with the high Vis light absorbance of $Ni(OH)_2$-NiOOH (*41*), which was confirmed by UV-Vis spectroscopy measurement, as shown in fig. S9 (A and B). The thin intermediate layer of Au that served to protect the underneath Ni from dissolution during the prolonged electroplating of $Ni(OH)_2$-NiOOH also had high Vis light absorbance (fig. S9B), and this further improved the actuation response of the actuator to Vis light. Figure S10 compares two actuators made by electroplating $Ni(OH)_2$-NiOOH for 0.5 hours on bare Ni and Au-coated Ni substrates, and the latter exhibited a higher change in curvature under illumination. In addition to using broad-band Vis light, the actuation response under narrowband Vis light with wavelengths of 400, 520, and 700 nm was also studied on an 8.5-mm-long actuator. The results in fig. S11 show similar curvature changes at these wavelengths, thus indicating that the actuation response is fairly consistent within the Vis light spectrum.

In such actuation responses, the actuator always moves in the forward direction that corresponds to contraction of the $Ni(OH)_2$-NiOOH layer. This is in contrast with the redox-induced electrochemical actuation behavior illustrated in fig. S3 and movie S1, in which the actuation under oxidation is in the forward direction but, under reduction, is in the backward direction, corresponding to the material expanding, as discussed above. The absence of the backward actuation under light illumination suggests that the actuation was not caused by the $Ni(OH)_2 \leftrightarrow$NiOOH redox reaction (*34*), and this also agrees well with the GIXRD result that the spectra of the material in both the oxidized and reduced states were not affected by Vis light illumination, as described above (fig. S7).

However, mass measurement in a quartz crystal microbalance (QCM) (fig. S12) revealed a mass increase in $Ni(OH)_2$-NiOOH as the QCM cell was moisturized and significant and reversible mass reduction and increment of the $Ni(OH)_2$-NiOOH every time the light illumination was switched on and off (Fig. 2B). As shown in Fig. 2C, without light triggering, the $Ni(OH)_2$-NiOOH in either the oxidized or reduced state also exhibits similar actuation in the forward direction on humidity reduction in the environment. The sensitivity to humidity caused an actuator to straighten and curl autonomously and quickly when it was reversibly placed onto and taken away from a wet sponge (movie S3), and this behavior is similar to that of recently described humidity-induced actuators (*42*–*44*). The QCM result and the humidity sensitivity here show that the desorption and absorption of water from the $Ni(OH)_2$-NiOOH material led to a significant and reversible actuation effect, and the light-induced actuation was likely the result of desorption of water molecules from the material upon light illumination, which decreased the mass of the material.

The results so far suggest a different light-induced water-desorption actuation mechanism in $Ni(OH)_2$-NiOOH, in addition to the already known electrochemical redox mechanism (*34*). The possibility of interplay between these two independent actuation mechanisms led to

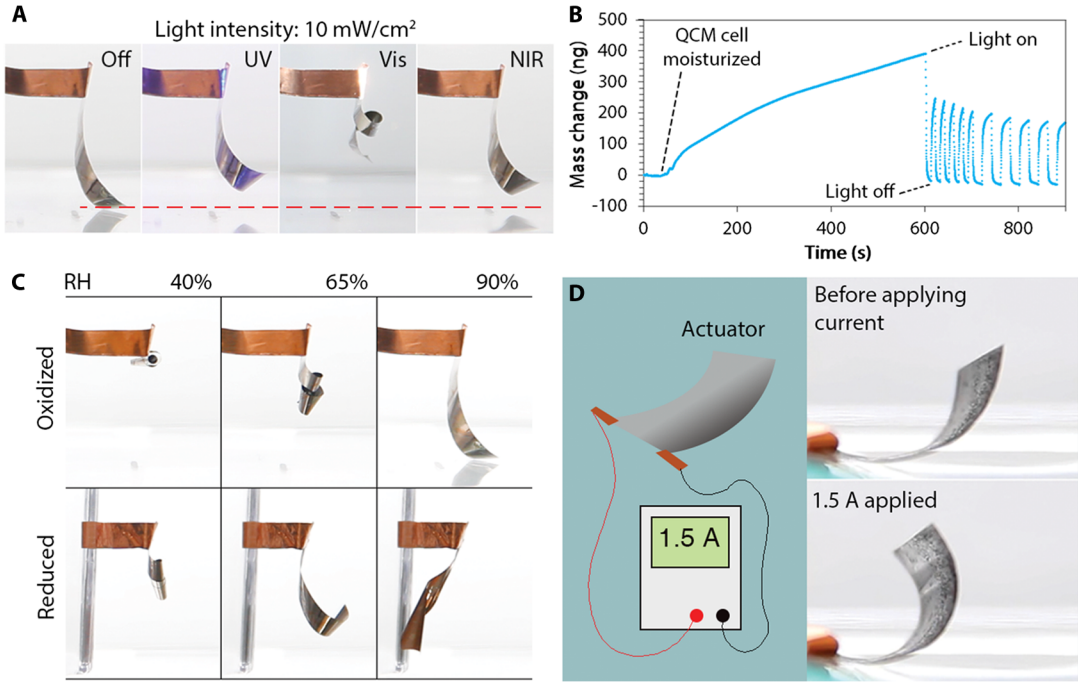

Fig. 2. Response of the actuator to different stimulations. (**A**) Actuation induced by UV, Vis, and NIR lights at 10 mW/cm^2. (**B**) QCM measurement of Ni(OH)$_2$-NiOOH showing a mass increase under humid environment and a mass decrease upon the light illumination. (**C**) Photos of the oxidized (top) and reduced (bottom) actuator at different RHs. (**D**) Schematic diagram of Joule heating experiment and the heat-induced actuation of an actuator with size of about 30 × 25 mm^2 under 1.5-A electrical current.

the finding that the shape of an actuator under ambient conditions can be controlled by an electrochemical treatment of the Ni(OH)$_2$-NiOOH layer. By a reduction treatment, the actuator shown in the lower row of Fig. 2C was significantly less curly than the oxidized counterpart under the same relative humidity (RH), and could undergo a larger actuation displacement when illuminated by Vis light of 5 mW/cm^2 at an RH of 65%, as shown in fig. S13.

In additional to using light to trigger desorption of water, thus leading to material contraction and hence forward actuation, heating up by an electric current can also produce the same effect. An electric current of 1.5 A was made to flow through the Cu tape at one edge of an actuator (30 mm × 25 mm) with the Ni(OH)$_2$-NiOOH layer facing up, and the resultant Joule heating caused a temperature rise of 2° to 5°C in the actuator, as measured by a thermocouple (Fig. 2D). As shown in movie S4, the actuator curled in the forward direction immediately after the current was turned on, and once the current was turned off, it flexed back to the original shape in a similar rate.

Performance of the light-induced actuation

Figure 3A shows the effect of the light intensity on the actuation. The actuator bent under Vis light at 5 mW/cm^2 and curled to form loops as the intensity was increased from 10 to 100 mW/cm^2. The actuation speed also increased with the intensity because full actuation would be completed in ~3 s regardless of the light intensity (movie S5). A bending/curling speed of 30°/s to 220°/s was achieved from 5 to 50 mW/cm^2 (Fig. 3B). At 100 mW/cm^2, the actuator curled to form two small loops within 1 s (movie S6), which corresponds to a speed of 400°/s; however, it took about 20 s to recover, which could have been caused by the slow water adsorption.

To calculate the actuating strain exerted by the Ni(OH)$_2$-NiOOH layer, the change in radius of curvature R of an actuator under actuation is needed. The coordinates (x, y) of the free end relative to the clamped end of an actuator at the initial and actuated states were measured from the recorded video, and the corresponding R was obtained by assuming the shape of the bent or curled actuator to be circular. For the milder actuation induced by Vis light of 5 mW/cm^2, R was calculated by a geometrical relation:

$$R = \frac{x^2 + y^2}{2x} \quad (1)$$

At illumination intensities of 10 to 100 mW/cm^2, the actuation became so severe that Eq. 1 is inapplicable. In such cases, R was obtained by dividing the length of the actuator L by 2π and the number of loops n that the actuator has curled into. Because a certain length L_o of the actuator might not have actuated because of the blockage of the light illumination, the length is subtracted by L_o so that $R = \frac{L - L_o}{2n\pi}$. For example, for the actuation under Vis light of 10 mW/cm^2 in Fig. 3A, n was observed to be 1, and L_o was measured to be about 4.3 mm. Similarly, for Vis light of 20, 50, and 100 mW/cm^2, n = 1.5, 2, and 3, and L_o = 3.0, 0.0, and 0.0 mm, respectively.

With R measured, the actuating strain can be calculated following a previous method that was derived from Hsueh (*45*) and Cheng and Ngan (*46*). As shown in Fig. 3C, the thickness of the actuating Ni(OH)$_2$-NiOOH layer and the substrate are t_a and t_s, and the boundary at the clamped end is the origin of the coordinate system (x, z). Under illumination, the actuating layer is assumed to be shortened uniformly by strain ε_i if it was freed from the substrate. This is the intrinsic actuating strain of the Ni(OH)$_2$-NiOOH layer if it stood alone in a stress-free strain similar to thermal strains. In reality, the strain of the whole actuator in the actuated state is ε, which decomposed into a uniform component and a bending component: $\varepsilon = c + \frac{z - t_b}{R}$, for $-t_s \le z \le t_a$, where c is the

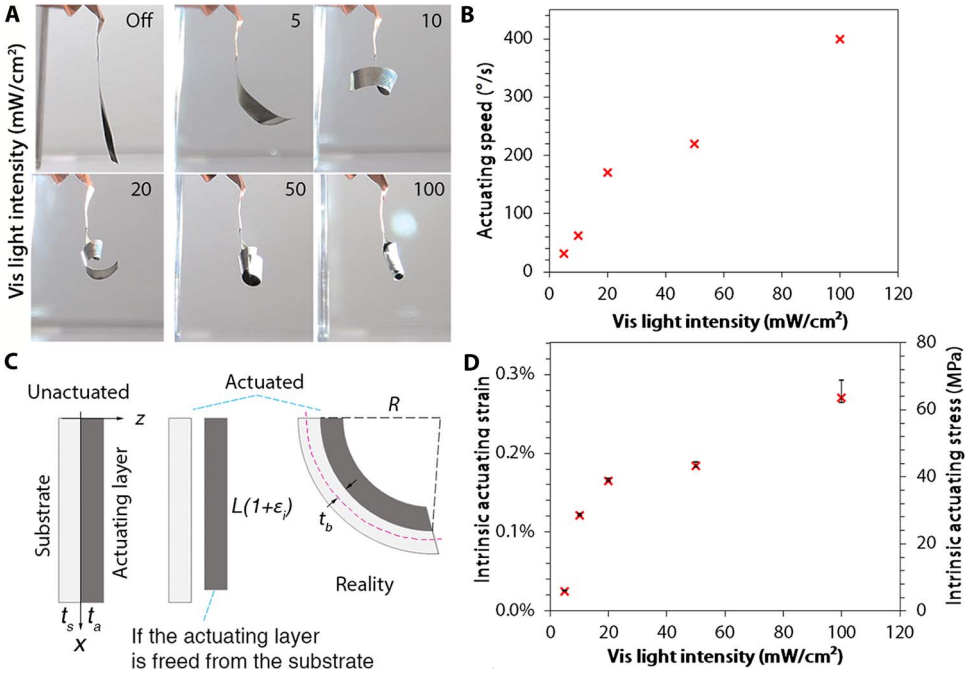

Fig. 3. Actuating properties of Vis light–induced actuation. (**A**) Vis light–induced actuation at increasing intensity from 5 to 100 mW/cm^2. (**B**) Actuating speed, measured in degrees per second, for the bending and curling of the actuator measured from individual actuation tests plotted against the Vis light intensity used. (**C**) Schematic diagram for the calculation of the intrinsic actuating strain of the Ni(OH)$_2$-NiOOH layer (not drawn to scale). Left: Unactuated state showing the coordinate system and the symbols for the dimensions. Middle: Intrinsic actuating strain ε_i under light illumination if the Ni(OH)$_2$-NiOOH actuating layer was freed from the substrate. Right: Actuation in reality as the Ni(OH)$_2$-NiOOH actuating layer bends forward to a radius of curvature *R*. (**D**) Calculated intrinsic actuating strain and stress of the Ni(OH)$_2$-NiOOH layer corresponding to the actuation plotted against Vis light intensity. The data points represent the mean value of the intrinsic actuating strain and stress obtained from the measurement of 10 cycles of actuation. The error bars show the values resulted from the range of the measurement.

uniform strain component and t_b is the position of the bending axis. The bending axis is defined as the line in the section where the bending strain component is zero, which is different from the conventional neutral axis where the normal stress is zero. The stress state in the actuating layer is given by $\sigma_a = E_a(\varepsilon - \varepsilon_i)$ and that in the substrate is $\sigma_s = E_s\varepsilon$.

Three boundary conditions are satisfied by the actuator. First, the resultant force due to the strain component is zero: $E_s t_s c + E_a t_a(c - \varepsilon_i) = 0$. Second, the resultant force due to the bending strain component is zero: $\int_{-t_s}^{0} \frac{E_s(z - t_b)}{R} dz + \int_{0}^{t_a} \frac{E_a(z - t_b)}{R} dz = 0$. Third, the sum of the bending moment with respect to the bending axis is zero: $\int_{-t_s}^{0} \sigma_s(z - t_b)dz + \int_{0}^{t_a} \sigma_a(z - t_b)dz = 0$, where E_s is taken as the elastic modulus of only the Ni because the Au layer is thin and E_a is that of the actuating layer. They were measured by nanoindentation (G200, Agilent) to be 220 ± 13 and 24 ± 5.6 GPa, respectively. Solving these conditions gives the three unknowns in the model:

$$c = \left(\frac{E_a t_a}{E_s t_s + E_a t_a}\right)\varepsilon_i \,,\; t_b = \frac{E_a t_a^2 - E_s t_s^2}{2(E_s t_s + E_a t_a)} \,,\; \text{and}$$

$$\varepsilon_i = \frac{1}{6R(t_a + t_s)}\left[\frac{E_a t_a^3}{E_s t_s} + \frac{E_s t_s^3}{E_a t_a} + 4\left(t_a^2 + t_s^2 + \frac{3t_a t_s}{2}\right)\right] \quad (2)$$

The actuating strain of the Ni(OH)$_2$-NiOOH layer based on *R* measured from 10 cycles of actuation is calculated by Eq. 2 to be 0.03 to 0.3% (Fig. 3D). The error bars refer to the measurement range of *R*, which increases over the actuation cycles due to the incomplete recovery of the actuator each time after the light was switched off. The incomplete recovery and, hence, the error bar are more significant at higher Vis light intensity; for 100 mW/cm^2, the recovery was not complete after 20 s. The intrinsic actuating stress of the Ni(OH)$_2$-NiOOH layer was calculated as $\sigma_i = E_a\varepsilon_i$ (Fig. 3D), and the intrinsic work density was calculated as $W_i = E_a\varepsilon_i^2/2$ (fig. S14). The magnitudes are in the order of 10 MPa and 10 kJ/m^3, respectively, which are comparable to mammalian skeletal muscles (*1*). The actuation is also highly repeatable, as demonstrated by a cyclic actuation test under Vis light at 20 mW/cm^2 for 5000 cycles (fig. S15 and movie S7).

The light-induced actuating force under periodic Vis light illumination at 10 mW/cm^2 was measured by a microtensile tester (fig. S16). The measured force was tensile, indicating that a contraction force was induced in the actuator so that the tensile tester had to exert a larger tensile force to continue the programmed displacement. The measurements under different preloads are plotted in Fig. 4A, in which the rises and drops of the force are synchronized with the on and off of the light. The force change represents the actuating force of the actuator, and as shown in Fig. 4B, this increases with the preload from 5 to 9 mN, likely due to the tautening of the curly actuator under a higher preload. From the actuating force measured by the microtensile tester, the corresponding actuating stress σ was calculated by dividing the force *F* by the cross-section area *A* (width × thickness) of the Ni(OH)$_2$-NiOOH layer, namely, $\sigma = F/A$, and the work density by $W = \sigma^2/(2E_a)$. Given that the width and thickness of the actuating layer were 4.0 mm and 1.0 μm, respectively, the actuating stress calculated from the force is in the range of 1.25 to 2.25 MPa. Taking the elastic modulus of the Ni(OH)$_2$-NiOOH layer to be 24 GPa, the work density is 33 to 105 J/m^3. These values of the actuating stress and work density are 10 and 100 times smaller than the intrinsic stress and work density of the Ni(OH)$_2$-NiOOH layer under the same light intensity (Vis light at 10 mW/cm^2) as reported above, because the stress and work density measured in the tensile tester are the overall performance of the entire actuator. Thus, the values are the performance of the actuating layer net of the elastic constraint of the Ni substrate, which has about the same thickness as the actuating layer but ~10 times higher elastic modulus (~220 GPa).

By plating at selected areas (fig. S1B), we plated three strips each with 2-mm width of Ni(OH)$_2$-NiOOH layer across the width on a substrate of 25 mm by 8 mm to form an actuator with three actuating hinges, as

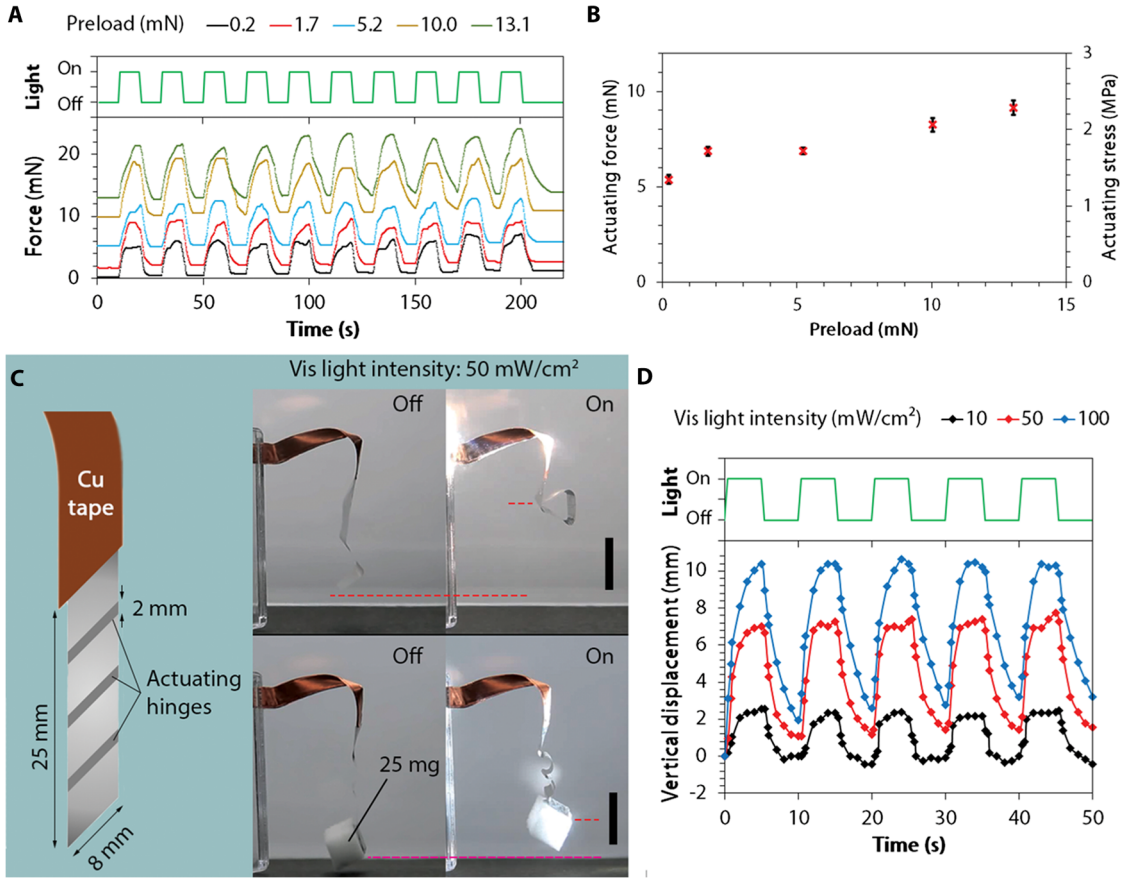

Fig. 4. Actuation performance induced by Vis light. (**A**) Change in force measured by a microtensile tester under periodic Vis light of 10 mW/cm^2 and (**B**) the corresponding actuating force and stress plotted against the preload. The data points represent the mean value of the force and stress obtained from the measurement of 10 cycles of actuation. The error bars show the values resulted from the range of the measurement. (**C**) Schematic diagram of an actuator with three actuating hinges fabricated by plating at selected areas, and the self-folding and weight-lifting actuation under Vis light at 50 mW/cm^2 (scale bars, 10 mm). (**D**) Vertical displacements of the weight-lifting actuation under different light intensities.

shown in the schematic diagram of Fig. 4C. Because the fabrication requires a quick immersion of the actuator into ethanol to remove the unwanted masks, the $Ni(OH)_2$-NiOOH layer was slightly reduced (*47*) and hence expanded, leading to a variation in the shape of the actuating hinges, as shown in the photo capture of Fig. 4C. Nevertheless, the hinges could actuate by a similar magnitude to cause the entire actuator to self-fold and lift weights (movie S8).

For the self-folding, the top hinge can lift the lower part of the actuator by a displacement of >15 mm under Vis light illumination at 50 mW/cm^2. When the free end was attached to a 25-mg load that was a small piece of polymeric sponge, the latter can be lifted by 2 to 10 mm by increasing the light intensity from 10 to 100 mW/cm^2 (Fig. 4D). This is equal to 8 to 40% of the length of whole actuator. From the weight-lifting experiment, the actuation performance exerted by the actuating layer can be calculated. The mass of the actuating hinges was estimated by multiplying the volume to the density. The thickness of the actuating layer was measured to be 1.2 to 1.4 μm, and the density was taken to be that of NiOOH, which is equal to 4.0 and 4.7 g/cm^3 for β-NiOOH and γ-NiOOH, respectively (*48*). The combined mass of the actuating hinges was estimated to be 0.24 to 0.31 mg, and they successfully lifted an object of 25 mg, which is ~100 times heavier than the actuating hinges themselves. However, the load lifted of 25 mgf or 0.25 mN here is an order of magnitude smaller than the actuation force measured by the microtensile tester, as shown in Fig. 4B. This is because the load lifted in Fig. 4C was a performance of the entire actuator device, which was a folded structure with three actuating hinges. As shown in Fig. 4C, whereas the actuating hinges could fold significantly under the activation of the light, the passive parts of the strip structure exhibited significant compliance under load, and this limited the weight that could be lifted. The intrinsic load-lifting capability of the present type of actuators is much larger in the order of 10 mN or 1 gf, as measured directly by tensile testing as shown in Fig. 4B. Figure 4D also shows that the recovery of the actuator was slower than the actuation response especially at high light intensities. Replotting Fig. 4D into fig. S17 by changing the abscissa into the change in time after each switching on or off of the light shows a faster actuation response compared with the recovery. The hysteresis is an indication of the difference in kinetics between water desorption and reabsorption from and to the actuating material.

Applications

The low Vis light intensity required for the actuation allows sunlight-induced actuation to be realized. To demonstrate this, we intentionally performed an experiment on a cloudy day with a weak solar intensity of ~15 mW/cm^2, and the constituent intensity for Vis light was measured to be a low value of ~5 mW/cm^2. An actuator was placed in a transparent

box covered by a shading cloth, as shown in Fig. 5A, and an actuation was triggered when the cloth was removed to let the actuator be exposed to sunlight (Fig. 5B and movie S9). The extent of the actuation was found to be similar to that triggered by the artificial light source used in the experiment in Fig. 3 at the same intensity (second panel in Fig. 3A). The result here demonstrates the possibility for an outdoor-usable solar actuator. Moreover, as shown above in Fig. 2C and fig. S13, the shape of an actuator at a given RH can also be changeable by a redox reaction pretreatment.

To demonstrate further potential applications, we fabricated various actuators by masked plating using chemical-resist stickers of different patterns (fig. S1C). Figure 5C shows a leaf-shaped actuator that "closes" under NIR light at 200 mW/cm^2 (movie S10), which biomimics the rapid leaf movement of a "sensitive plant" (*49*, *50*). Moreover, Fig. 5D and movie S11 show bundles of actuator strips that will stand and fall upon the turning off and on of Vis light of 50 mW/cm^2, which mimics the response of hairs under temperature change driven by arrector pili muscles. The actuation of the "hairs" was likely complicated by shadowing or inter-illumination, and if many actuators have to be activated simultaneously for certain applications, then a light-guiding mechanism would be needed.

Last, a walking bot with a front and a back leg was created by selectively plating two actuating hinges, each 2 mm wide, along the width of the underlying Ni substrate strip. As mentioned above, the quick immersion of an actuator into ethanol to remove the unwanted masks caused the $Ni(OH)_2$-NiOOH layer to slightly expand, which resulted in a convex actuating hinge. Because the hinges were facing up, by immersing the hinge at the back leg into ethanol for a longer time than that at the front, we made the back-leg hinge expand more so that the back leg became more vertical than the front leg, as shown in the schematic diagram of Fig. 5E. This asymmetry caused the front leg to move further than the back leg when illuminated by horizontal flashing Vis light of 50 mW/cm^2, as shown in the photo captures in Fig. 5E, thus making the bot walk toward the light (movie S12). Movie S13 shows another walking bot made by longer immersion of the actuator in ethanol to achieve more convex shapes of the two actuating hinges. Between the two actuating hinges, a light blocker was also erected so that, when light was incident at a horizontal angle, only one of the two actuating hinges would be illuminated because of the shadowing effect of the light blocker. As shown in movie S13, irrespective of the light direction relative to the orientation of the walking bot, only the hinge that was illuminated was actuated, making the device always walk toward the light.

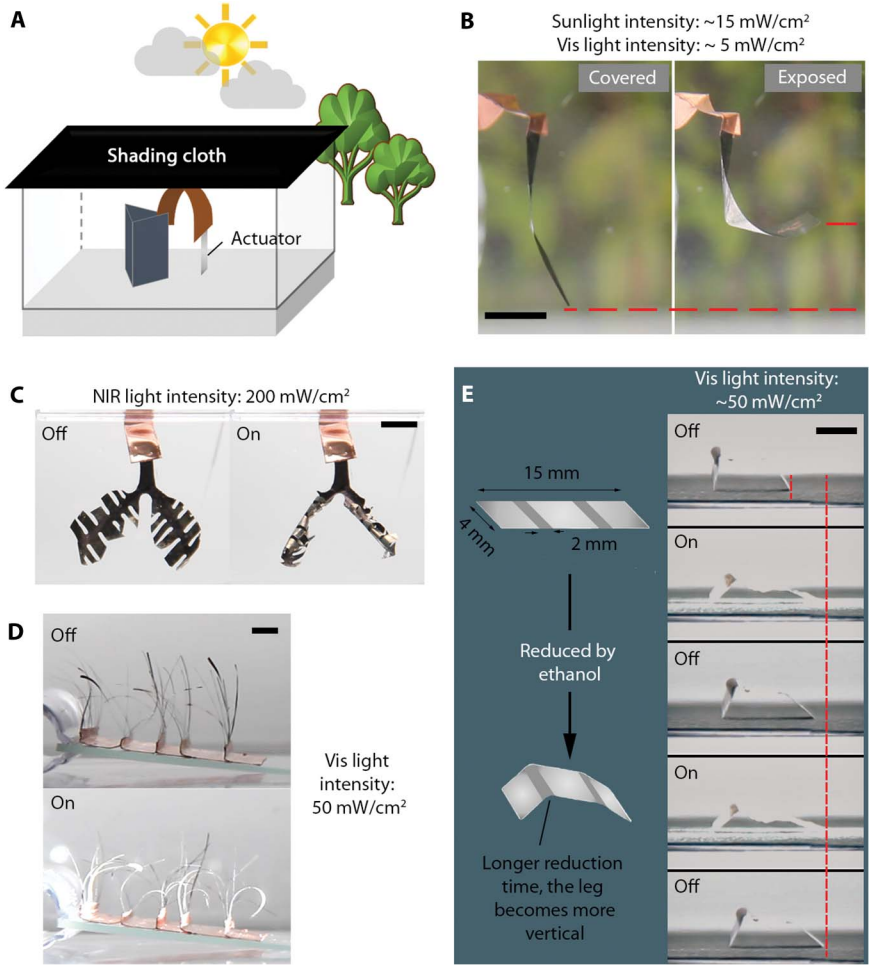

Fig. 5. Potential applications of the light-induced actuator. (**A**) Schematic diagram of the sunlight-induced actuation experiment and (**B**) demonstration of the sunlight-induced actuation at ~15 mW/cm^2. (**C**) Biomimicked sensitive plant under NIR light of 200 mW/cm^2 and (**D**) hairs by patterned plating under Vis light of 100 mW/cm^2. (**E**) Schematic diagram of an actuator with two hinges that serves as a walking bot capable of walking toward flashing Vis light of ~50 mW/cm^2. Scale bars, 5 mm.

DISCUSSION

In this work, we have introduced a light-triggered actuating material system, turbostratic $Ni(OH)_2$-NiOOH, that is capable of producing significant and fast actuation by water desorption when illuminated by low-intensity light. Film actuators with different shapes can be fabricated by electroplating the material on a passive substrate, and they are capable of bending and curling reversibly by Vis light illumination at low intensities. The high intrinsic actuating stress and response rate of the material system are comparable to mammalian skeletal muscles. With these properties, we have fabricated wireless actuating devices that are capable of self-folding and weight lifting and also demonstrated sunlight-induced actuation, biomimicking actuation, and a walking bot that are wirelessly stimulated. In addition, through an independent mechanism of a volume-changing electrochemical redox reaction, the shape of the fabricated actuator can be varied, which is of great importance for outdoor applications in which thin-film actuators in general can be sensitive under the ambient conditions.

The Vis light–induced actuation property of $Ni(OH)_2$-NiOOH makes it an important addition to the known group of light-induced artificial muscles (*16*–*27*) that are mainly functional under UV and NIR light, which is more harmful than Vis light. In addition, Vis light sources with low intensities are easily available and much cheaper, and this is another advantage of the material.

To further develop the present type of Vis light–induced actuators, scaling up the actuating $Ni(OH)_2$-NiOOH layer is desirable. However, the thickness of the $Ni(OH)_2$-NiOOH layer was limited to ~1 μm by the present fabrication method based on electroplating. Instead, a large number of actuators can be combined together to give a large total actuation force. As mentioned above, shadowing or inter-illumination among actuators may become an issue, but this can be overcome by designing a proper light guiding or delivery system to uniformly distribute light to all actuators. Nevertheless, as the present results show, a single or a few actuators may already serve the purpose for microrobot applications. Another promising research direction is scaffolding by lithography or three-dimensional printing to produce origami or kirigami actuators, with the help of computer-aided design and finite element analysis. With these configurations of the actuator, other modes of actuation, for example, twisting and rotation, might also be achieved. The present results on the intrinsic actuating properties may provide the necessary data for such developments.

MATERIALS AND METHODS

This study aims at developing a type of Vis light–induced actuators based on the actuating material system $Ni(OH)_2$-NiOOH. Here, the fabrication of the actuators, materials characterization, the actuation tests, and the demonstration of potential applications are described.

Chemicals and materials

Three solution baths were prepared for the electroplating of Ni, Au, and $Ni(OH)_2$-NiOOH. A commercial Ni-plating kit (Caswell Inc.) was used for the Ni bath, and an Oromerse SO Part B (Technic Inc.) electroless plating solution was used for making the Au bath. All the other chemicals were purchased from Sigma-Aldrich and were used without further purification. Fluorine-doped tin oxide (FTO)–coated glass slides (3 mm thick; sheet resistance, ~10 ohms/square) were purchased from Sigma-Aldrich. Chemical-resist stickers (50 μm thick; CM-200E) were purchased from MAX Bepop, and copper (Cu) tape was purchased from 3M. Deionized (DI) water with a resistivity of ~18 megohms·cm was used to make all the solution baths and for rinsing.

Three-step electroplating fabrication of $Ni(OH)_2$-NiOOH film actuator

The procedure is shown in the schematic diagram in fig. S1A. First, Ni was electroplated on FTO glass masked by a chemical-resist sticker with rectangular openings (the typical size was 20 mm by 4 mm), using a constant cathodic current of −15 mA/cm^2 for 7.5 min in the Ni bath in a two-electrode electrochemical cell against a Ni metal sheet counter electrode. Because prolonged plating of $Ni(OH)_2$-NiOOH might lead to dissolution of the Ni substrate, a protective Au layer was electroplated on the Ni. The Au bath was composed of Oromerse SO Part B and 1.7 M sodium sulfite (Na_2SO_3) in the volume ratio of 1:9, and a constant cathodic current density of −0.1 mA/cm^2 was applied to the Ni-plated FTO in a three-electrode cell against a silver/silver chloride (Ag/AgCl)–saturated reference electrode and a platinum (Pt) mesh counter electrode for 30 min. The color of the plated Au layer was uniform and dull. Last, $Ni(OH)_2$-NiOOH was anodically plated on the substrate in a solution bath of 0.13 M nickel sulfate ($NiSO_4$), 0.1 M sodium acetate (CH_3COONa), and 0.13 M sodium sulfate (Na_2SO_4) in a three-electrode cell. The current density was 0.4 mA/cm^2 against saturated calomel reference electrode and Pt mesh counter electrode for 2 hours under vigorous stirring. The plated $Ni(OH)_2$-NiOOH was in an oxidized state with a gray color. After each plating process, the sample and the FTO glass were rinsed with DI water and dried with a compressed air duster. After the three-step electroplating process, the chemical-resist sticker was removed, and the resultant film actuator was peeled off the FTO glass by a pair of sharp tweezers. For the rectangular actuators with the size of 20 mm by 4 mm, one end of the film actuator was adhered to a piece of Cu tape so that it could be clamped for the electrochemical treatment and actuation tests. This reduced the exposed size of the actuator to about 18 mm by 4 mm.

Plating at selected areas and patterned plating methods

For plating at selected areas, the procedure is shown in the schematic diagram in fig. S1B. First, after Ni was plated on FTO glass, designated positions were painted with a permanent marker pen. The unmasked regions were plated with the Au and $Ni(OH)_2$-NiOOH layer with the same conditions as above, except that the current density applied for plating $Ni(OH)_2$-NiOOH was increased to 0.55 mA/cm^2. Then, the paint was removed by ethanol. This resulted in actuating hinges for self-folding, weight lifting, and a walking bot in Figs. 4C and 5E. Patterned plating for making biomimicking actuators was carried out by using chemical-resist stickers of various shapes, as shown in fig. S1C.

Electrochemical reduction treatment and characterization of the $Ni(OH)_2$-NiOOH actuator

An LK2006A electrochemical workstation (Lanlike) was used for applying potential to actuators under a bath of 1 M NaOH solution. To prevent any contact of the Cu tape to the solution, a thin coating of lacquer was applied to the tape. For the reduction treatment, −0.4 V was applied to an actuator against an Ag/AgCl reference electrode and a Pt mesh counter electrode in 1 M NaOH for 2 hours. After this treatment, the color of the $Ni(OH)_2$-NiOOH material was found to change from gray to golden. CV characterization of $Ni(OH)_2$-NiOOH was performed in the same LK2006A workstation. An actuator was immersed in 1 M

NaOH, where a potential scan from 0.2 to 0.55 V was applied to the actuator at a rate of 10 mV/s.

Materials characterization of $Ni(OH)_2$-NiOOH

Scanning electron imaging and EDS were carried out in a LEO 1530 FEG scanning electron microscope. Samples were prepared by directly cutting small pieces from film actuators and adhered them to sample holders. For imaging, the samples were gold-palladium–sputtered for 20 s in a Bal-Tec SCD 005 Sputter Coater. For EDS, no sputtering was performed.

TEM imaging and SAED were carried out in an FEI Tecnai G^2 20 S-TWIN STEM. Samples were prepared by first plating $Ni(OH)_2$-NiOOH onto an FTO glass, with the same solution bath and current conditions described above, except that the plating time was reduced to 40 min. The plated $Ni(OH)_2$-NiOOH was in an oxidized state with dark color. Samples in the reduced state were prepared by electrochemical reduction under 1 M NaOH, with 0 V applied against an Ag/AgCl reference electrode for 30 min. Then, the $Ni(OH)_2$-NiOOH on the FTO glass was scratched off by sharp tweezers and adhered to a TEM Cu grid with carbon film wetted with DI water.

GIXRD was performed in a Rigaku SmartLab 9-kW x-ray diffractometer. Samples were prepared by plating $Ni(OH)_2$-NiOOH on Ni-plated FTO glasses for 40 min. The Ni could prevent the diffraction from the FTO that would mask the peaks for $Ni(OH)_2$-NiOOH. Reduced samples were prepared at the same condition as the TEM samples above. Samples supported on FTO glass were put directly onto the sample holder of the diffractometer. Parallel-beam/parallel-slit analyzer mode was used, with the incidence angle for the x-ray beam being 0.5° and the sweep rate being 1°/min at steps of 0.1°.

Light-induced actuation tests

Actuation tests were performed inside a compartment illuminated by low-intensity light-emitting diode light as background for video recording. An actuator was put into a tightly sealed transparent chamber at a temperature of 22° to 24°C. The background lighting has little effect on the light-induced actuation, as shown in fig. S8. By putting desiccant and wet sponge into the chamber, RH levels of 40 and 90% were obtained respectively after 0.5 to 1 hour, as measured by a Tes-1360A humidity/temperature meter (TES Electrical Electronic Corp.). Without the desiccant or wet sponge, the RH was about 65%. The humidity-induced actuation demonstrated in movie S3 was performed in an open space.

To trigger the actuation, we used a xenon arc lamp LSH-X150 connected to a power supply LSP-X150 (Zolix Instruments Co. Ltd) with light filters (Shenzhen Fuzhe Technology Co. Ltd) to illuminate NIR, Vis, and UV light. The wavelength was checked by a spectrometer (HR2000 + CG, Ocean Optics) to be 800 to 1100 nm, 400 to 700 nm, and 300 to 500 nm, respectively. Vis light with narrowband wavelengths of 400, 520, and 700 nm was provided by applying relevant narrowband filters together with the Vis light filter. The intensities of the filtered lights were measured by a TES11333 solar power meter (TES Electrical Electronic Corp.) and were varied through adjusting the distance between the light source and the meter.

UV-Vis spectroscopy of $Ni(OH)_2$-NiOOH and Au

UV-Vis diffusive reflectance spectroscopy was carried out in a Lambda 35 UV-Vis spectrophotometer (PerkinElmer) with an integrating sphere. The samples studied included a bare FTO glass plate, $Ni(OH)_2$-NiOOH electroplated on a FTO glass plate, and Au electroplated on a FTO glass plate. The electroplating methods were the same as those described above.

Mass measurement of water adsorption/desorption of $Ni(OH)_2$-NiOOH

The mass change of $Ni(OH)_2$-NiOOH under light illumination and humid environment was measured by a CHI430B electrochemical quartz crystal microbalance (CH Instruments Inc.). A piece of Au-plated quartz crystal was electroplated with $Ni(OH)_2$-NiOOH for 30 min. The test environment was moisturized by putting water droplets into the QCM cell, and periodic Vis light illumination was applied at 30 mW/cm^2 (fig. S12).

Measurement of actuation force induced by light

To measure the light-induced actuating force, we adhered an actuator to Cu tapes at both ends and clamped onto an Agilent T150 Universal Testing Machine (UTM) microtensile tester with micronewton resolution and under periodic Vis light illumination at ~10 mW/cm^2, as shown in fig. S16. Because the tensile tester was not enclosed, the humidity was not controlled, and the RH was measured to be 50 to 55% during the test. A very slow strain rate, 1×10^{-6}/s, was used so that the actuator was only stretched by 0.01 to 0.1% during the test and could be assumed in a quasi-static state. The tester would start measuring the force and displacement when a preset sensing force was reached, which contributed to the part of the preload.

SUPPLEMENTARY MATERIALS

robotics.sciencemag.org/cgi/content/full/3/18/eaat4051/DC1

Fig. S1. Schematic diagrams of the fabrication of the actuators.
Fig. S2. Cyclic voltammogram of the actuator under 1 M NaOH.
Fig. S3. Electrochemical actuation under 1 M NaOH.
Fig. S4. SEM images of the top view of an actuator.
Fig. S5. EDS mapping of the cross section of an actuator.
Fig. S6. SAED of oxidized and reduced $Ni(OH)_2$-NiOOH.
Fig. S7. GIXRD spectrum of oxidized and reduced $Ni(OH)_2$-NiOOH.
Fig. S8. Experimental setup for the light-induced actuation tests.
Fig. S9. Light absorption spectra measured by UV-Vis spectroscopy.
Fig. S10. Comparison of light-induced actuation of actuators with Ni and Ni-Au substrate under Vis light.
Fig. S11. Actuation tests under Vis light at narrowband wavelengths.
Fig. S12. Schematic diagram of the QCM cell.
Fig. S13. Shape control of the actuator by redox reactions under the same RH.
Fig. S14. Intrinsic actuating work density of the $Ni(OH)_2$-NiOOH layer plotted against the Vis light intensity.
Fig. S15. Long-term stability test of the intrinsic actuating strain.
Fig. S16. Schematic diagram of the UTM tensile tester for the actuating force measurement under periodic Vis light illumination.
Fig. S17. Vertical displacement of the weight-lifting actuation plotted against the change in time after light on/off.
Movie S1. Electrochemical actuation of an actuator.
Movie S2. Light-actuation of an actuator by UV, Vis, and NIR light.
Movie S3. A demonstration of the humidity sensitivity of an actuator.
Movie S4. A demonstration of the Joule heating–induced actuation of an actuator.
Movie S5. Light-actuation of an actuator induced by Vis light at 5 to 50 mW/cm^2.
Movie S6. Light-actuation of an actuator induced by Vis light at 100 mW/cm^2 with slow motion.
Movie S7. Cyclic actuation test of an actuator for 5000 cycles.
Movie S8. A demonstration of a hinged actuator capable of self-folding and weight lifting under Vis light.
Movie S9. A demonstration of the sunlight-induced actuation of an actuator.
Movie S10. A demonstration of a mimicked sensitive plant with rapid leaf movement.
Movie S11. A demonstration of mimicked hairs that stand and fall under light stimulation.
Movie S12. A demonstration of a walking bot under a horizontal flashing Vis light source.
Movie S13. A demonstration of the shadowing effect on a walking bot under a horizontal flashing Vis light source.

REFERENCES AND NOTES

1. J. D. W. Madden, N. A. Vandesteeg, P. A. Anquetil, P. G. A. Madden, A. Takshi, R. Z. Pytel, S. R. Lafontaine, P. A. Wieringa, I. W. Hunter, Artificial muscle technology: Physical principles and naval prospects. *IEEE J. Ocean. Eng.* **29**, 706–728 (2004).
2. P. Brochu, Q. Pei, Advances in dielectric elastomers for actuators and artificial muscles. *Macromol. Rapid Commun.* **31**, 10–36 (2010).
3. R. H. Baughman, Conducting polymer artificial muscles. *Synth. Met.* **78**, 339–353 (1996).
4. M. Shahinpoor, Y. Bar-Cohen, J. O. Simpson, J. Smith, Ionic polymer-metal composites (IPMCs) as biomimetic sensors, actuators and artificial muscles—A review. *Smart Mater. Struct.* **7**, R15 (1998).
5. T. F. Otero, J. M. Sansieña, Soft and wet conducting polymers for artificial muscles. *Adv. Mater.* **10**, 491–494 (1998).
6. R. H. Baughman, C. Cui, A. A. Zakhidov, Z. Iqbal, J. N. Barisci, G. M. Spinks, G. G. Wallace, A. Mazzoldi, D. De Rossi, A. G. Rinzler, O. Jaschinski, S. Roth, M. Kertesz, Carbon nanotube actuators. *Science* **284**, 1340–1344 (1999).
7. E. W. H. Jager, E. Smela, O. Inganäs, Microfabricating conjugated polymer actuators. *Science* **290**, 1540–1545 (2000).
8. E. Smela, Conjugated polymer actuators for biomedical applications. *Adv. Mater.* **15**, 481–494 (2003).
9. J. Weissmüller, R. N. Viswanath, D. Kramer, P. Zimmer, R. Würschum, H. Gleiter, Charge-induced reversible strain in a metal. *Science* **300**, 312–315 (2003).
10. J. Foroughi, R. N. Viswanath, D. Kramer, P. Zimmer, R. Würschum, H. Gleiter, Torsional carbon nanotube artificial muscles. *Science* **334**, 494–497 (2011).
11. M. Acerce, E. K. Akdoğan, M. Chhowalla, Metallic molybdenum disulfide nanosheet-based electrochemical actuators. *Nature* **549**, 370–373 (2017).
12. T. Kim, L. Zhu, R. O. Al-Kaysi, C. J. Bardeen, Organic photomechanical materials. *ChemPhysChem* **15**, 400–414 (2014).
13. S. M. Mirvakili, I. W. Hunter, Artificial muscles: Mechanisms, applications, and challenges. *Adv. Mater.* **30**, 1704407 (2018).
14. S. Palagi, A. G. Mark, S. Y. Reigh, K. Melde, T. Qiu, H. Zeng, C. Parmeggiani, D. Martella, A. Sanchez-Castillo, N. Kapernaum, F. Giesselmann, D. S. Wiersma, E. Lauga, P. Fischer, Structured light enables biomimetic swimming and versatile locomotion of photoresponsive soft microrobots. *Nat. Mater.* **15**, 647–653 (2016).
15. M. J. Villangca, D. Palima, A. R. Bañas, J. Glückstad, Light-driven micro-tool equipped with a syringe function. *Light Sci. Appl.* **5**, e16148 (2016).
16. M.-H. Li, P. Keller, B. Li, X. Wang, M. Brunet, Light-driven side-on nematic elastomer actuators. *Adv. Mater.* **15**, 569–572 (2003).
17. Y. Yu, M. Nakano, T. Ikeda, Photomechanics: Directed bending of a polymer film by light. *Nature* **425**, 145 (2003).
18. M.-H. Li, P. Keller, Artificial muscles based on liquid crystal elastomers. *Philos. Trans A Math. Phys Eng. Sci.* **364**, 2763–2777 (2006).
19. S. Kobatake, S. Takami, H. Muto, T. Ishikawa, M. Irie, Rapid and reversible shape changes of molecular crystals on photoirradiation. *Nature* **446**, 778–781 (2007).
20. C. L. van Oosten, D. Corbett, D. Davies, M. Warner, C. W. M. Bastiaansen, D. J. Broer, Bending dynamics and directionality reversal in liquid crystal network photoactuators. *Macromolecules* **41**, 8592–8596 (2008).
21. C. L. van Oosten, C. W. M. Bastiaansen, D. J. Broer, Printed artificial cilia from liquid-crystal network actuators modularly driven by light. *Nat. Mater.* **8**, 677–682 (2009).
22. S. Iamsaard, S. J. Aßhoff, B. Matt, T. Kudernac, J. J. L. M. Cornelissen, S. P. Fletcher, N. Katsonis, Conversion of light into macroscopic helical motion. *Nat. Chem.* **6**, 229–235 (2014).
23. K. Iwaso, Y. Takashima, A. Harada, Fast response dry-type artificial molecular muscles with [c2]daisy chains. *Nat. Chem.* **8**, 625–632 (2016).
24. W. Wu, L. Yao, T. Yang, R. Yin, F. Li, Y. Yu, NIR-light-induced deformation of cross-linked liquid-crystal polymers using upconversion nanophosphors. *J. Am. Chem. Soc.* **133**, 15810–15813 (2011).
25. J. Loomis, B. King, T. Burkhead, P. Xu, N. Bessler, E. Terentjev, B. Panchapakesan, Graphene-nanoplatelet-based photomechanical actuators. *Nanotechnology* **23**, 045501 (2012).
26. M. Ji, N. Jiang, J. Chang, J. Sun, Near-infrared light-driven, highly efficient bilayer actuators based on polydopamine-modified reduced graphene oxide. *Adv. Funct. Mater.* **24**, 5412–5419 (2014).
27. J. Mu, C. Hou, H. Wang, Y. Li, Q. Zhang, M. Zhu, Origami-inspired active graphene-based paper for programmable instant self-folding walking devices. *Sci. Adv.* **1**, e1500533 (2015).
28. S. Lu, B. Panchapakesan, Optically driven nanotube actuators. *Nanotechnology* **16**, 2548–2554 (2005).
29. O. M. Tanchak, C. J. Barrett, Light-induced reversible volume changes in thin films of azo polymers: The photomechanical effect. *Macromolecules* **38**, 10566–10570 (2005).
30. Z. Cheng, T. Wang, X. Li, Y. Zhang, H. Yu, NIR–Vis–UV light-responsive actuator films of polymer-dispersed liquid crystal/graphene oxide nanocomposites. *ACS Appl. Mater. Interfaces* **7**, 27494–27501 (2015).
31. S. Serak, N. Tabiryan, R. Vergara, T. J. White, R. A. Vaia, T. J. Bunning, Liquid crystalline polymer cantilever oscillators fueled by light. *Soft Matter* **6**, 779–783 (2010).
32. F. Cheng, R. Yin, Y. Zhang, C.-C. Yen, Y. Yu, Fully plastic microrobots which manipulate objects using only visible light. *Soft Matter* **6**, 3447–3449 (2010).
33. J. O. Besenhard, *Handbook of Battery Materials* (John Wiley & Sons, 2008).
34. K.-W. Kwan, N.-Y. Hau, S.-P. Feng, A. H.-W. Ngan, Electrochemical actuation of nickel hydroxide/oxyhydroxide at sub-volt voltages. *Sens. Actuators B* **248**, 657–664 (2017).
35. C. Faure, C. Delmas, M. Fouassier, Characterization of a turbostratic α-nickel hydroxide quantitatively obtained from an $NiSO_4$ solution. *J. Power Sources* **35**, 279–290 (1991).
36. P. Oliva, J. Leonardi, J. F. Laurent, C. Delmas, J. J. Braconnier, M. Figlarz, F. Fievet, A. de Guibert, Review of the structure and the electrochemistry of nickel hydroxides and oxy-hydroxides. *J. Power Sources* **8**, 229–255 (1982).
37. D. Tench, L. F. Warren, Electrodeposition of conducting transition metal oxide/hydroxide films from aqueous solution. *J. Electrochem. Soc.* **130**, 869–872 (1983).
38. D. Singh, Characteristics and effects of γ-NiOOH on cell performance and a method to quantify it in nickel electrodes. *J. Electrochem. Soc.* **145**, 116–120 (1998).
39. D. S. Hall, D. J. Lockwood, C. Bock, B. R. MacDougall, Nickel hydroxides and related materials: A review of their structures, synthesis and properties. *Proc. Math. Phys. Eng. Sci.* **471**, 20140792 (2015).
40. J. Biscoe, B. E. Warren, An X-ray study of carbon black. *J. Appl. Phys.* **13**, 364–371 (1942).
41. F. Hahn, B. Beden, M. J. Croissant, C. Lamy, *In situ uv* visible reflectance spectroscopic investigation of the nickel electrode-alkaline solution interface. *Electrochim. Acta* **31**, 335–342 (1986).
42. M. Ma, L. Guo, D. G. Anderson, R. Langer, Bio-inspired polymer composite actuator and generator driven by water gradients. *Science* **339**, 186–189 (2013).
43. H. Arazoe, D. Miyajima, K. Akaike, F. Araoka, E. Sato, T. Hikima, M. Kawamoto, T. Aida, An autonomous actuator driven by fluctuations in ambient humidity. *Nat. Mater.* **15**, 1084–1089 (2016).
44. B. Shin, J. Ha, M. Lee, K. Park, G. H. Park, T. H. Choi, K.-J. Cho, H.-Y. Kim, Hygrobot: A self-locomotive ratcheted actuator powered by environmental humidity. *Sci. Robot.* **3**, eaar2629 (2018).
45. C.-H. Hsueh, Modeling of elastic deformation of multilayers due to residual stresses and external bending. *J. Appl. Phys.* **91**, 9652–9656 (2002).
46. C. Cheng, A. H. W. Ngan, Reversible electrochemical actuation of metallic nanohoneycombs induced by pseudocapacitive redox processes. *ACS Nano* **9**, 3984–3995 (2015).
47. A. Kowal, S. N. Port, R. J. Nichols, Nickel hydroxide electrocatalysts for alcohol oxidation reactions: An evaluation by infrared spectroscopy and electrochemical methods. *Catal. Today* **38**, 483–492 (1997).
48. Q. Xu, T. Kobayashi, *Advanced Materials for Clean Energy* (CRC Press, 2015).
49. J. Braam, In touch: Plant responses to mechanical stimuli. *New Phytol.* **165**, 373–389 (2005).
50. A. G. Volkov, L. O'Neal, M. I. Volkova, V. S. Markin, Morphing structures and signal transduction in *Mimosa pudica* L. induced by localized thermal stress. *J. Plant Physiol.* **170**, 1317–1327 (2013).

Acknowledgments: We thank F. Y. F Chan for the operation of TEM, and Y. T. Huang for the operation of QCM and UV-Vis. **Funding:** This work was funded by a grant from the Research Grants Council (project no. 17206114) of the Hong Kong Special Administrative Region and the Kingboard Endowed Professorship in Materials Engineering. **Author contributions:** K.W.K. and A.H.W.N. conceived the idea, designed the experiments, and wrote the manuscript. K.W.K., S.J.L., and N.Y.H performed the experiments. All the authors contributed materials and/or tools and analyzed the data. **Competing interests:** The authors declare that they have no competing interests. **Data and materials availability:** All data needed to support the conclusions of this manuscript are included in the main text or the Supplementary Materials. Contact K.W.K. for materials.

Submitted 23 February 2018
Accepted 3 May 2018
Published 30 May 2018
10.1126/scirobotics.aat4051

Citation: K. W. Kwan, S. J. Li, N. Y. Hau, W.-D. Li, S. P. Feng, A. H. W. Ngan, Light-stimulated actuators based on nickel hydroxide-oxyhydroxide. *Sci. Robot.* **3**, eaat4051 (2018).

Science Robotics

Light-stimulated actuators based on nickel hydroxide-oxyhydroxide

K. W. Kwan, S. J. Li, N. Y. Hau, Wen-Di Li, S. P. Feng, and Alfonso H. W. Ngan

Sci. Robot. **3** (18), eaat4051. DOI: 10.1126/scirobotics.aat4051

Science Robotics (ISSN 2470-9476) is published by the American Association for the Advancement of Science. 1200 New York Avenue NW, Washington, DC 20005. The title *Science Robotics* is a registered trademark of AAAS.